Electrochimica Acta 242 (2017) 227–239

Contents lists available at ScienceDirect

Electrochimica Acta

journal homepage: www.elsevier.com/locate/electacta

Research Paper

A platform for *in situ* Raman and stress characterizations of V_2O_5 cathode using MEMS device

Hyun Jung[a,b,c], Konstantinos Gerasopoulos[a,c,1], A. Alec Talin[d], Reza Ghodssi[a,b,c,*]

[a] MEMS Sensors and Actuators Laboratory (MSAL), University of Maryland, College Park, MD 20742, USA
[b] Department of Electrical and Computer Engineering, University of Maryland, College Park, MD 20742, USA
[c] Institute for Systems Research, University of Maryland, College Park, MD 20742, USA
[d] Sandia National Laboratories, Livermore, CA 94551, USA

ARTICLE INFO

Article history:
Received 27 September 2016
Received in revised form 19 April 2017
Accepted 28 April 2017
Available online 1 May 2017

Keywords:
lithium-ion battery
in situ characterization
Raman spectroscopy
stress
microstructure

ABSTRACT

We present an *in situ* approach for the characterization of lithium intercalation/deintercalation in thin-film Li-ion battery electrodes. The method allows simultaneous measurement of microstructural changes during lithiation using micro-Raman (μRaman) spectroscopy in parallel with stress changes *via* optical interferometry. We observe evolution in the microstructure and stress in the various crystal phases in the Li-V-O system, including both reversible and irreversible phase transitions. We also correlate spectral shifts in certain Raman active modes with changes in the electrode stress, and thus confirm previously hypothesized origins of these observations. Ultimately, the combined stress/μRaman *in situ* technique can be leveraged as a characterization platform for a wide variety of electrode materials for advancing battery performance.

1. Introduction

Lithium-ion batteries (LIBs) provide high energy density while being compact and light-weight and are the most pervasive energy storage technology powering portable electronic devices such as smartphones, laptops, and tablet PCs. At the same time, new electric transportation systems including hybrid electric vehicles, plug-in hybrid electric vehicles, and fully electric vehicles are becoming more and more important. These vehicles require rechargeable batteries with even higher energy density and cycle life as well as improved safety and lower cost [1]. Considerable work have been made to develop new electrode materials that maximize capacity and long cycle life. A key challenge in these work have been characterizing the complex physico-chemical processes occurring during operation in various LIB electrode materials. As part of these efforts, Cabana et al. reviewed different conversion reaction based metal oxides, sulfides, nitrides, phosphides, and fluorides [2]. Baddour-Hadjean and Pereira-Ramos focused on Raman spectroscopy method for characterizing lithium metal and carbon-based electrode, transition metal oxide-based compounds, and phospho-olivine $LiFePO_4$ compound [3], while Reddy et al. extensively reviewed metal oxides and oxysalts as anode materials for LIBs [4]. Most LIB electrode materials react with Li-ions *via* intercalation into interstitial sites or channels within the host lattice or by alloying mechanism with the electrode material [5,6]. While it is generally accepted that the repeated strain/stress cycles play a role in the long-term capacity loss, the detailed mechanisms still remain unclear [3,7–9]. Therefore, development of techniques which are capable of capturing in real time the microstructural changes and the associated stress during operation are crucial for unraveling the LIB degradation mechanisms and further improving the LIB performance.

While *ex situ* methods have yielded a great deal of information for understanding underlying LIB function and degradation processes under static conditions, the true dynamics of LIB operation can be best revealed *via in situ* methods as the battery system operates (*in operando*). Recently, various *in situ* or *in operando* analysis methods have been utilized in order to understand the mechanical strain/stress changes in LIB electrodes [10–15]. Among these, the multi-beam optical sensor (MOS) has proven to be an effective method for characterizing the stress evolution in LIB thin film electrodes during cycling. In the MOS technique, a silicon wafer is coated with a passivation layer, a current collector, and a thin film active battery material of interest. The stress generated in the active battery material during lithium

* Corresponding author at: 2173 A.V. Williams Bldg, University of Maryland, College Park, MD 20742, USA.
E-mail address: ghodssi@umd.edu (R. Ghodssi).
[1] Present address: The Johns Hopkins University Applied Physics Laboratory LLC, 11100 Johns Hopkins Road, Laurel, MD 20723, USA.

http://dx.doi.org/10.1016/j.electacta.2017.04.160
0013-4686/

cycling induces curvature in the wafer which is measured by an array of parallel laser beams. Change in curvature is determined by measuring the relative change in the spacing between the reflected beams, and the stress is calculated using the Stoney equation. This method enables the measurement of the average stress, biaxial modulus and fracture energy for both silicon thin film and commercial electrodes [8,9,14,16]. While the technique has proven to be advantageous for mechanical characterization, the limited ability to directly access the electrode restricts its potential integration with other methods that could provide microstructural and chemical composition information. Also, the stress value determined using this method represents an average over the entire wafer-scale area. Thus, the MOS technique is suitable for materials that experience spatially homogeneous structural changes over this length scale (typically tens of centimeters).

In addition to stress, significant advances have been achieved in *in situ* microstructural characterization of LIB electrodes. For example, *in situ* transmission electron microscopy (TEM) provides direct imaging of the microstructural changes of individual nanowire or nanoparticle electrodes with near-atomic resolution in real time [17–19]. Crystallographic changes which occur inside the battery electrode as it is lithiated and delithiated have also been investigated using *in situ* X-ray diffraction [20–23] (XRD) and absorption methods [20,24]. Recently, Liu et al. utilized a soft X-ray absorption spectroscopy technique for revealing distinct Li-ion and electron dynamics attributed to charge conductivity, phase transformation mechanism, and mesoscale morphology in $LiCo_{1/3}Ni_{1/3}Mn_{1/3}O_2$ and $LiFePO_4$ electrodes [25]. *In situ* nuclear magnetic resonance spectroscopy and neutron scattering have also been applied to study structural changes in silicon electrodes [26,27] and a large format LIB [28], respectively. Compared to the aforementioned techniques, which rely on bulky external equipment and complex electrochemical cells, μRaman spectroscopy is an alternative tool for probing structural and chemical variations in LIB electrodes in a relatively simple fashion and with high spatial resolution [3,29,30]. Information that can be gleaned using Raman

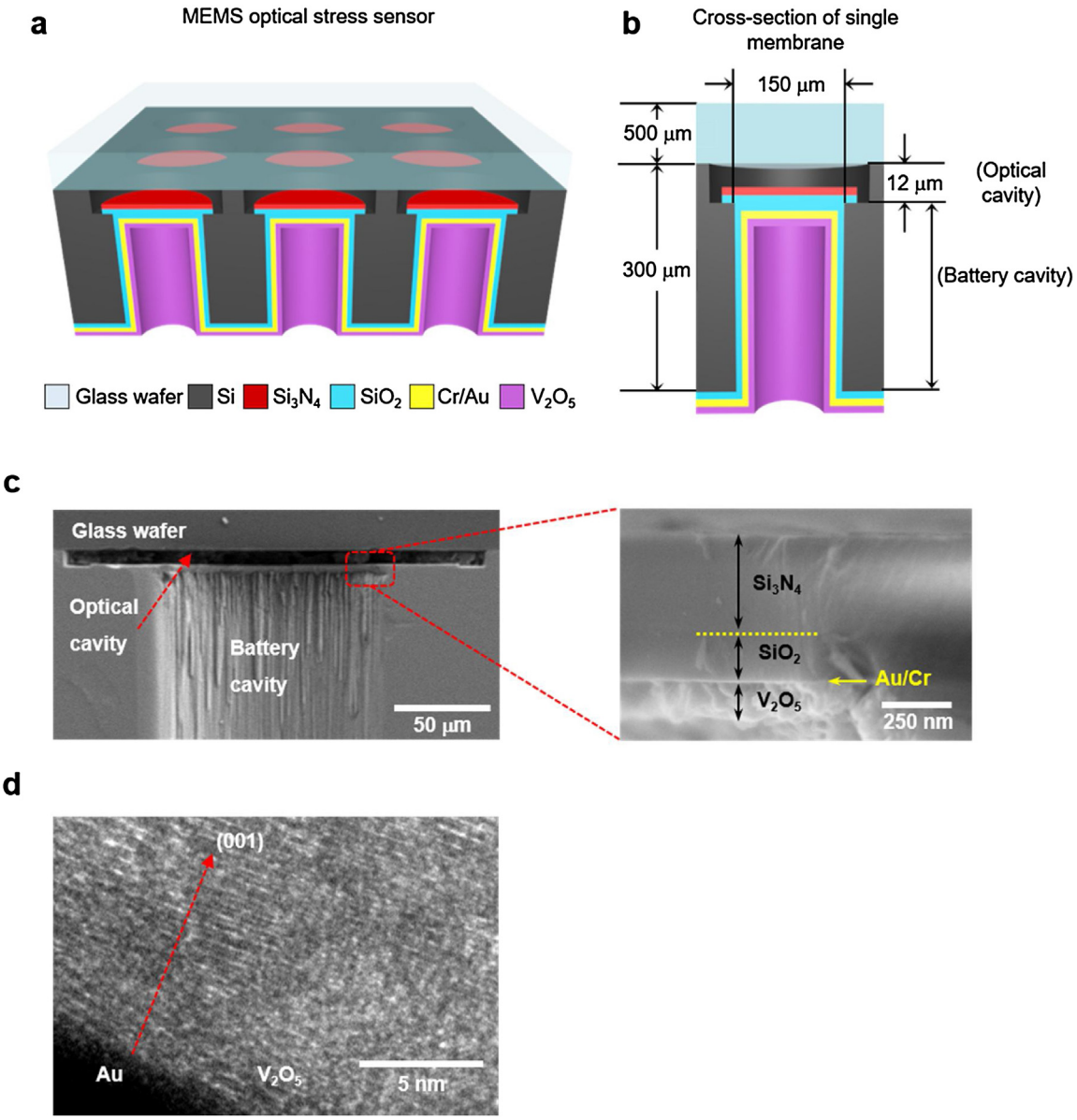

Fig. 1. MEMS optical stress sensor geometry. (a) 3D schematic of MEMS optical stress sensor. (b) Cross-section diagrams of a single membrane (not drawn to scale). (c) Left panel: Cross-section SEM image of the membrane in the MEMS optical stress sensor. Right panel: Enlarged view of the membrane, showing multi-layer structure. (d) TEM image of a V_2O_5 layer grown on top of Au layer.

includes crystallinity/disorder, strain, and composition, including Li content [3,31]. *In situ* Raman spectroscopy has been applied to various anode and cathode materials including graphite [32], transition metal oxides [29,33–37], and phospho-olivine $LiFePO_4$ [30], providing rich structural and chemical information relevant to the lithiation mechanisms [3]. Combining *in situ* μRaman spectroscopy with stress measurement could provide additional insights into the battery operation and degradation mechanisms such as identification of which phases are present during abrupt changes in stress.

In this work, we have developed a platform, in which a microelectromechanical systems (MEMS) based optical stress sensor is integrated with μRaman spectroscopy enabling *in situ* characterization of both the qualitative stress and microstructural changes in a thin film LIB electrode over multiple charge/discharge cycles. An interferometric method is applied to analyze stress evolution, including observation of phase transitions. Throughout this work, vanadium pentoxide (V_2O_5) thin film is selected as a model electrode to demonstrate capabilities of the platforms. V_2O_5 is an attractive material as cathode in LIB due to its high capacity. It can accommodate up to three lithium ions per mole of oxide, providing a specific capacity of 450 mAh/g within the voltage range from 1.5–4 V [3]. As the electrochemical performance of LIB electrodes are strongly dependent on the structural changes caused by the lithium insertion/extraction process and different preparation conditions [38], considerable efforts have been made to study the structural dependent characteristics of V_2O_5 and its lithiated $Li_xV_2O_5$ phases, which make it suitable for verifying the feasibility of the platform. Our results reveal that the stress induced during lithium insertion/extraction is asymmetric with respect to the preferred crystallographic orientation of the $Li_xV_2O_5$ thin film electrodes, consistent with previous structural analyses [3]. This *in situ* stress and Raman measurements confirm the puckering in the V_2O_5 planes during early lithiation followed by

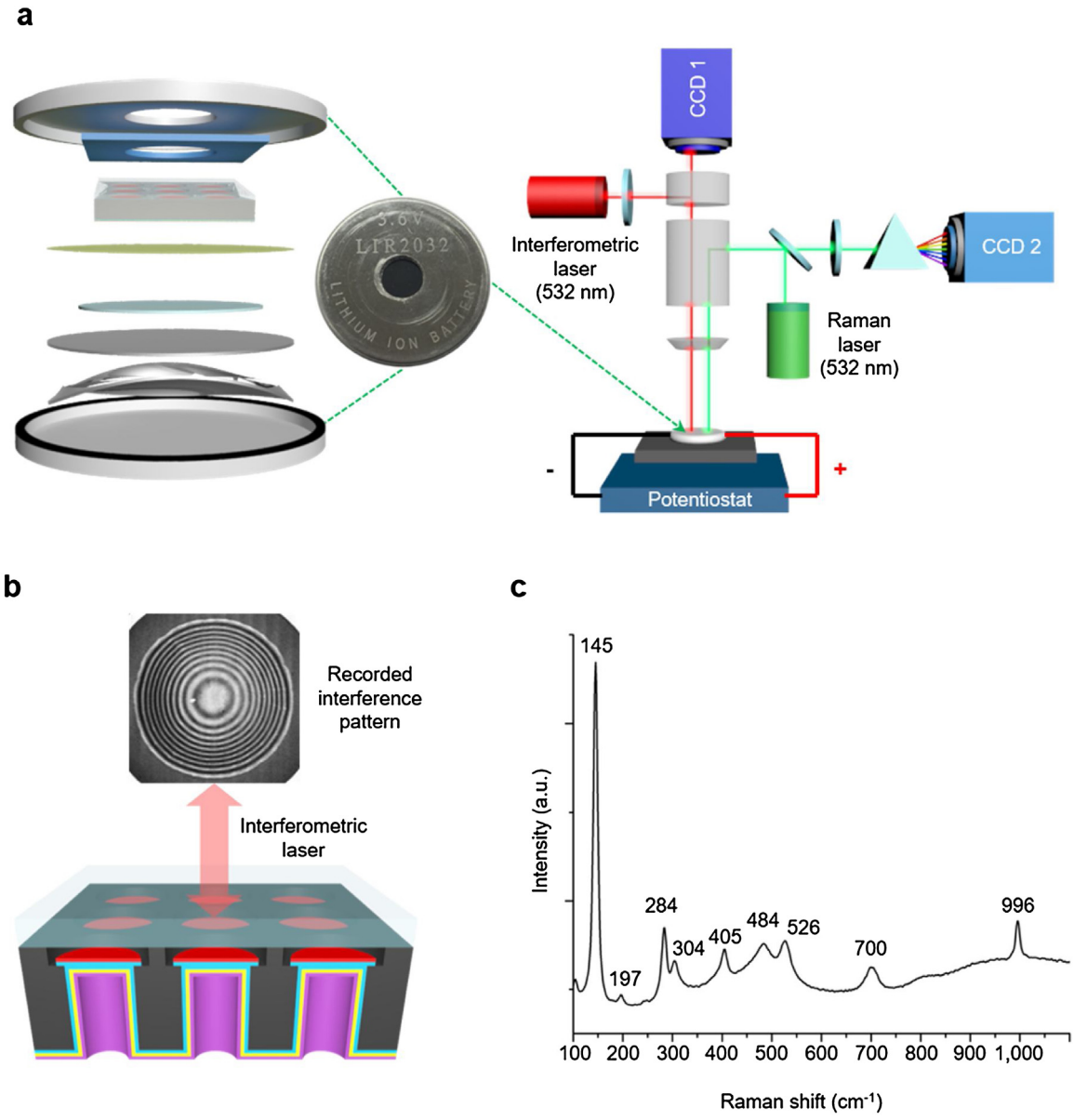

Fig. 2. Schematic illustration. (a) Schematic of the coin cell parts (from top to bottom: cathode cap, adhesive tape, MEMS optical stress sensor, separator, lithium anode, stainless steel, spring, and anode cap) for *in situ* experiment and simplified schematic diagrams of the experimental setup showing the location of the coin cell under test relative to the Raman microscope. (b) Optical image of the experimentally obtained interference pattern from the membrane. (c) Experimentally obtained Raman spectrum of as-deposited V_2O_5 thin film electrode underneath the glass wafer and membrane.

irreversible formation of highly disordered rocksalt-type structure upon further discharge. Additionally, low frequency Raman peak shifts associated with long range vibrations are correlated to specific changes in stress confirming earlier hypothesis regarding the origin of these shifts.

2. Method and experimental

2.1. MEMS optical stress sensor design

Fig. 1a shows our MEMS optical stress sensor, composed of an array of mechanically flexible circular membranes. The membranes separate the sensor into two cavities, referred to as the 'optical' and 'battery' cavities. The optical cavity is created by anodically bonding glass and silicon wafers. The deeper battery cavity is formed on the other side of the membrane, enabling the deposition of an insulating layer, current collector and cathode/anode material, as well as providing a channel for the liquid electrolyte. We selected thin film V_2O_5 as a cathode material to demonstrate the capability of our approach. The detailed fabrication procedure is described in our previous work [39] (see Supplementary Fig. 1 for simplified fabrication process). Fig. 1b illustrates the cross-section of a single membrane with 150 μm diameter, formed by the 700 nm thick Si_3N_4 and 200 nm thick SiO_2

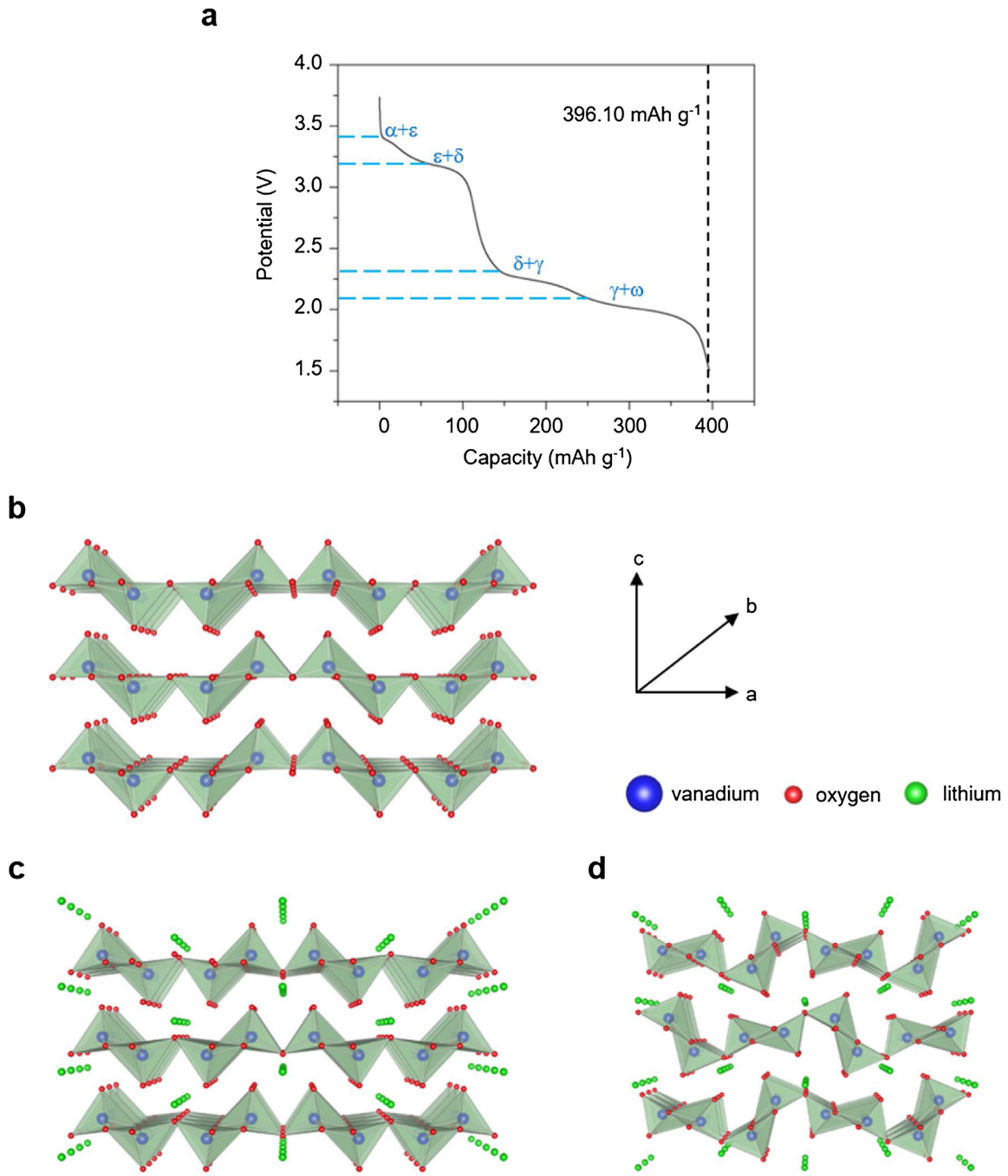

Fig. 3. Electrochemical discharge curve of ALD-deposited V_2O_5 thin film electrode in the customized cell and schematic representation of the electrochemically produced $Li_xV_2O_5$ structure. (a) Galvanostatic Li-ion insertion curve at C/12 rate. Phase-transformation plateaus at 3.4 V (α- to ε-phase), 3.2 V (ε- to δ-phase), 2.3 V (δ- to γ-phase), and 2.05 V (γ- to ω-phase) are observed (labeled in blue). (b-d) Perspective view of the $Li_xV_2O_5$ structure in different phases: (b) α-phase, (c) δ-phase, and (d) γ-phase.

layers inside the 12 μm deep optical cavity. Inside the 288 μm deep battery cavity, a 50 nm thick SiO_2 is used as a barrier coating to prevent lithium intercalation into the silicon wafer, followed by thin layers of Cr/Au as the current collector. Finally, a 137 nm thick V_2O_5 thin film electrode (0.81 Å per cycle) is conformally coated as the cathode material by atomic layer deposition (ALD). The cross-section scanning electron microscope (SEM) image of the fabricated sensor is shown in Fig. 1c. Additional structural and compositional characterizations of the membrane shown in Supplementary Fig. 2 indicate well-defined, uniformly coated various layers inside the battery cavity. It has been reported previously that the V_2O_5 film shows preferential growth along (001) direction on an Au-coated stainless steel [40]. This preferential growth on the Au-coated membrane is confirmed using transmission electron microscopy (TEM) (Fig. 1d) and by X-ray diffraction (XRD) (Supplementary Fig. 3).

The optical cavity of the sensor is utilized for monitoring the membrane deflection due to the stress change in the electrode using optical interferometry. At the same time, the optical cavity allows μRaman spectroscopy to probe the V_2O_5 thin film electrode layer through the transparent glass wafer and the multi-layer membrane, which is sufficiently thin to be semi-transparent. Thus, this unique design of the sensor addresses the challenge of *in situ* characterization of both the stress and structural changes during battery operation.

2.2. Coin cell assembly

A modified coin cell with an optical window is devised to facilitate the experiment during battery operation. The optical window (5 mm in diameter) is machined into the coin cell cap, and double-sided adhesive aluminum foil tape (1170 tape, 3 M) is placed in between the cathode cap and the MEMS optical stress sensor (Fig. 2a). The hermetic sealing of the coin cell is achieved using the aluminum foil tape with conductive adhesive to interface the sensor to the conductive top coin cell manifold for proper battery operation. The optical cavity side of the MEMS optical stress sensor is positioned to face the optical window of the coin cell and the cell is assembled in an argon-filled glove box. A polymer separator (Celgard 3501) soaked in lithium-conducting electrolyte (1 M $LiPF_6$ solution in ethyl carbonate/dimethyl carbonate (EC/DMC, 1:1 by volume), Novolyte Technologies) is placed on top of the MEMS optical stress sensor, and metallic lithium is included as the counter electrode to form a lithium half-cell. After the cell is closed in the glove box, all experiments are carried out in air under normal ambient conditions. The assembly of the coin cell has been demonstrated in our previous work [39] and evaluated again in this work (Fig. 3).

2.3. Experimental set-up

The assembled coin cell is connected to the potentiostat and placed under the Raman microscope (Yvon Jobin LabRam ARAMIS, Horiba, Ltd.) for a galvanostatic cycling test (Fig. 2a). The white-light illumination source of the Raman microscope is replaced with a despeckled laser (Fig. 2a, 532 nm interferometric laser) for interferometric measurement of the membrane deflection [39,41]. By employing the interferometric method, the same microscope used for the μRaman spectroscopy analysis can be used to collect information on the membrane deflection, thus enabling multi-modal, real-time monitoring in a unified setup.

When the interferometric laser illuminates one of the membranes in the optical cavity of the sensor, it produces an interference pattern (Fig. 2b). The as-fabricated sensor membranes have some residual stress associated with the fabrication and the anodic bonding processes which result in upward curvature [39] (See Supplementary Fig. 1). Due to this pre-deflected circular membrane, the initial interference pattern already shows multiple concentric rings [41]. The Raman laser (532 nm Nd:YAG laser) is used as the excitation source for μRaman spectroscopy measurements to probe the V_2O_5 electrode underneath the membrane. A 10 × objective is used to focus the Raman laser onto the electrode surface (spot size ~6.76 μm^2) and the spectra are measured in a back-scattering configuration. To avoid local heating of the electrode, the power of the laser beam is adjusted with a neutral density filter. Each spectrum is recorded for 30 seconds with three accumulations. The Raman spectrum of the as-deposited V_2O_5 thin film exhibits nine peaks in the 100–1000 cm^{-1} range, located at 145, 197, 284, 304, 405, 484, 526, 700, and 996 cm^{-1} (Fig. 2c), in agreement with previously reported Raman spectra [42], indicating that the excitation laser penetrates the glass wafer and the semi-transparent multi-layer membrane to probe the V_2O_5 electrode underneath.

The assembled cell is connected to a potentiostat (COMPACTSTAT, Ivium Technologies) and galvanostatic lithium cycling experiment is conducted. The imaging software installed on the computer connected to the Raman microscope supports automation functions controlled by user specific operations programmed in Visual Basic Script. This enables automatic switching between the two laser sources repeatedly throughout the experiment and computerized recording of the corresponding data. The recorded interference pattern and Raman spectra are automatically saved in the computer.

2.4. Fringe radius change

To analyze the stress changes in the V_2O_5 electrode during lithiation, the recorded interference patterns are processed using MATLAB. First, the interference pattern of the pristine electrode is compared to the interference patterns of the electrode under testing (Supplementary Fig. 4a). Each of the interference patterns is composed of multiple concentric rings and the edge of the inner most ring is utilized to track the radius change (fringe radius change, Supplementary Fig. 4b). In our previous work, it was verified that the fringe radius change varies linearly with the stress residing in the membrane [39] ($R^2 = 0.987$). Therefore, expansion of the fringe radius is denoted with a positive sign, and corresponds to compressive stress, with negative values conversely indicating tensile stress.

3. Results and discussion

3.1. In situ *visualization of structural changes of V_2O_5 electrode*

The MEMS optical stress sensor coated with ALD-deposited V_2O_5 thin film electrode is first used to evaluate the electrochemical properties of the V_2O_5 inside the modified coin cell (Fig. 3a). The discharge curve shows several resolved plateaus corresponding to well-known phase transitions during lithiation of V_2O_5 [3,43,44]. The α-, ε-, δ-, γ-, ω-V_2O_5 phases are identified within the voltage range from 3.75 to 1.5 V according to the following equation: $V_2O_5 + xe^- + xLi^+ \leftrightarrow Li_xV_2O_5$ with $0 < x \leq 3$. The α- to ε-phase and ε- to δ-phase transformation plateaus appeared at 3.4 and 3.2 V, respectively. Then the δ- to γ-phase and γ- to ω-phase transitions are observed at the 2.3 and 2.05 V plateaus, respectively. The observed electrochemical behavior validates that the customized cell is functional both in terms of its design to provide good electrical contacts to the cathode layers, as well as adequate hermetic seal such that the cell can be reliably operated in the ambient.

In Fig. 3b–d, we show schematically the structural transformations in $Li_xV_2O_5$ as x increases from 0 to ~3, corresponding to

the series of α- to ω-phases [43–45]. During lithiation, the structure of the $Li_xV_2O_5$ layer remains stable in the α-, ε-, and δ-phases (Fig. 3b and c). However, a light puckering of the V_2O_5 layers is observed in the δ-phase (Fig. 3c) due to the decrease in the *a* lattice parameter [43] (Table 1). When the voltage reaches the 2.3 V plateau ($1 < x < 2$ in $Li_xV_2O_5$), the δ-phase is transformed into the γ-phase, a substantially distinct structure (Fig. 3d). While the V_2O_5 layers remain perpendicular to the *c*-axis, the Li-ions are shifted along the *a*-axis direction and the puckering of the V_2O_5 layers becomes more pronounced as the *a* lattice parameter further contracts [3,43,45]. Finally, when the voltage reaches the 2.05 V plateau ($x > 2$), the γ-phase is irreversibly transformed into the ω-phase.

Fig. 4a displays galvanostatic discharge-charge curves of the ALD-deposited V_2O_5 thin film electrode at a current of 4.563 μA in three different voltage windows. These voltage ranges are chosen in order to induce different phase transitions in the $Li_xV_2O_5$ electrode [3,43,44]. The first window (3.75–2.8 V) corresponds to the reversible α-, ε-, and δ-phase transitions and the pristine V_2O_5 phase is recovered upon lithium extraction [3]. In this voltage range, the pristine V_2O_5 structure remains intact except for a minor puckering occurring along the *a* axis (Fig. 3b and c). However, in the second window (3.75 – 2.1 V) the δ-phase is transformed into the metastable γ-phase at 2.3 V. This transformation is accompanied by irreversible structural changes in the $Li_xV_2O_5$ film. The third window (3.75–1.5 V) leads to a weakly crystallized ω-phase with a tetragonal [46] or cubic [47] structure when the voltage reaches the 2.05 V plateau. Corresponding to Fig. 4a, differential capacity curves (*dQ/dV vs. V*) are presented in Fig. 4c–e. Differential capacity analysis enables observation of the potentials at which the majority of charge going into or out of an electrode over a given voltage increment [48]. This technique also offers greater sensitivity in probing cell degradation over a cycle life test [49].

Within the first window of 3.75 to 2.8 V where the pure V_2O_5 layer structure is preserved, the optical interference patterns from the circular membrane remain relatively symmetric (Fig. 4b(1), (2), (3)), as expected since there are no significant asymmetric contractions in the V_2O_5 lattice (Table 1). The differential capacity plot in this voltage window (Fig. 4c) also displays almost perfectly overlapping curves between the first and second cycles, indicating no major degradation in the electrode. In the second window (3.75–2.1 V) the δ-phase is transformed into the γ-phase with pronounced puckering of the V_2O_5 layers. This structural change is reflected as loss in symmetry in the interference pattern (Fig. 4b (4)). Given that the δ- to γ-phase transition is irreversible [43], it is not surprising that the interference pattern remains asymmetrical, even as the potential is cycled back to 3.75 V (Fig. 4b(5)). This irreversible structural change is also evidenced in the differential capacity plot (Fig. 4d). The peak height located at 2.3 V (Fig. 4d, denoted in star) is significantly reduced and shifted to the right in the fourth cycle after the irreversible structural change in the third cycle. Additionally, all the peak heights in the differential capacity curve are observed to decrease in the fourth cycle, indicating the degradation in the electrode [49]. A video showing the evolution of the interference pattern from the δ- to γ-phase is available as Supplementary Video 1. In the third window (3.75–1.5 V), $Li_xV_2O_5$ is transformed from the γ- to the ω-phase with significant structural rearrangement [44], which is again captured well by the evolution of the interference patterns during the lithiation process (Fig. 4b(6), (7), (8)). The previously observed asymmetric interference patterns becomes even more pronounced due to the further asymmetric contraction in the *a* lattice parameters during the δ- to γ-phase transition. However, after when the γ-phase is completely transformed into the ω-phase, the *a* and *b* lattice parameters becomes equal, resulting in the recovery of the symmetric interference pattern (Fig. 4b(8)). Since the ω-phase is irreversible, the symmetric interference pattern remains unchanged throughout further electrochemical cycling (Fig. 4b(9), (10)). The differential capacity plot displays a dramatic change after the transformation to the ω-phase (Fig. 4e). The peaks observed in the fifth cycle discharge process are disappeared and resulted in much broader peaks in the sixth cycle, showing a sign of an amorphous structure which we discuss in more detail later. The video showing the evolution of the interference patterns during the γ- to ω-phase transformation is available as Supplementary Video 2. These results demonstrate how structural changes in electrode material during lithiation can be optically imaged in real time using our *in situ* experimental platform. This visualization is enabled by the unique design of the optical stress sensor, which has the thin and flexible membrane inside the optical cavity, which allows monitoring of significant structural evolution in the electrode by merely observing the series of interference pattern images recorded during the experiment.

3.2. In situ *analysis of qualitative stress*

Correlation between the stress change and electrochemical discharge-charge of the first two cycles (Fig. 4a, first voltage window) are show in Fig. 5a and b. Upon lithium intercalation, the stress in the electrode becomes more tensile. This result can be explained in accordance with changes in the *a* and *b* lattice constants of the $Li_xV_2O_5$. As previously shown in Fig. 1d, the V_2O_5 film has a preferred (001) orientation with respect to the membrane. Therefore, changes in the *c* parameter do not affect the stress in the membrane since it is free to expand. However, elongation (contraction) in the *a* and *b* lattice parameters result in an increasing compressive (tensile) stress. Previous XRD studies have shown that the *a* lattice parameter continuously decreases as $Li_xV_2O_5$ changes from α- to δ-phase while the *b* parameter remains relatively constant (Table 1). This agrees with our observed increase in the tensile stress in the electrode. Inflections in the stress-potential curves such as regions I and II in Fig. 5b likely correspond to α- to ε-phase and ε- to δ-phase transitions which we discuss in more detail later. Upon lithium extraction, the stress returns its initial value.

Analysis on the stress change and electrochemical discharge-charge of the third and fourth cycles (Fig. 4a, second voltage window) are shown in Fig. 5c and d, with similar stress change upon discharge as seen in Fig. 5a and b. However, further lithiation (discharge) alters this trend with stress becoming more compressive stress (Fig. 5c, region I). This can be attributed to the elongation of the *a* lattice parameter during the δ- to γ-phase

Table 1
Lattice constants change reported in the literature for different phases of $Li_xV_2O_5$ characterized using XRD.

Lattice parameters	$Li_xV_2O_5$					
	x = 0.0 (α-V_2O_5)	x = 0.4 (ε-V_2O_5)	x = 1.0 (δ-V_2O_5)	x = 1.4 (δ-V_2O_5)	x = 2.0 (γ-V_2O_5)	x = 3.0 (ω-V_2O_5)
a (Å)	11.51 [3], 11.51 [50]	11.38 [3], 11.44 [50]	11.24 [3], 11.26 [50]	11.42 [50]	9.69 [3]	4.1 [44]
b (Å)	3.56 [3,50]	3.57 [3,50]	3.60 [3,50]	3.57 [50]	3.60 [3]	4.1 [44]
c (Å)	4.37 [3], 4.38 [50]	4.52 [3], 4.50 [50]	9.91 [3], 4.96 [50]	4.96 [50]	10.67 [3]	4.1 [44]

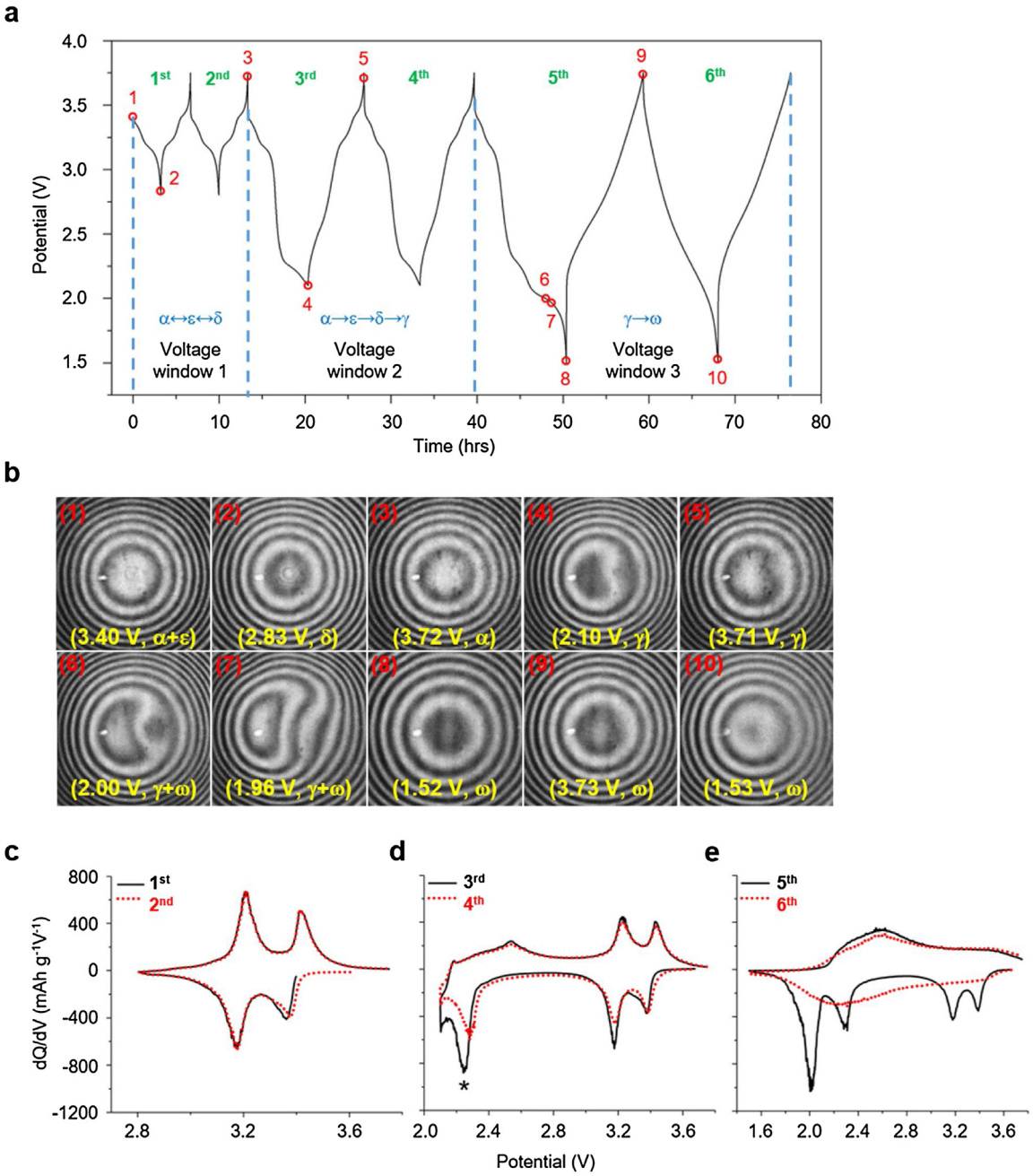

Fig. 4. Electrochemical discharge-charge, differential capacity curves of the different voltage windows, and corresponding interference pattern images. (a) Galvanostatic discharge-charge cycling curve of the ALD-deposited V_2O_5 electrode achieved from the *in situ* experimental setup. The phase transitions corresponding to the voltage windows are specified in blue. Red circles correspond to the point where the interference patterns are recorded. Cycle numbers are specified in green. (b) Series of experimentally obtained interference patterns collected along the discharge-charge curve (red circles) indicated with the potential and phase (in yellow). Initial deformation of symmetric interference pattern is observed (4), followed by dramatic interference pattern change (6-7), and symmetric interference pattern is recovered (8). (c, d, and e) Differential capacity curves of first and second, third and fourth, and fifth and sixth cycles. *Start denotes δ- to γ-phase transformation plateau in the third cycle.

transformation [50]. However, upon further discharge, the stress in the electrode becomes more tensile (Fig. 5c, region II). This change coincides with the pronounced puckering of the V_2O_5 layer in the γ-phase (Fig. 3d) due to the contraction in the *a* lattice parameter (Table 1), as indicated by the emergence of the asymmetric interference pattern (Supplementary Fig. 5). Upon charge, the same trend is observed as the relative stress returns to its initial value. The fourth cycle exhibits a similar stress change as observed for the third cycle (Fig. 5d), even though the $Li_xV_2O_5$ electrode is transformed from δ- to γ-phase. This indicates that the overall V_2O_5 layer structure is generally preserved in the γ-phase compared to the δ-phase structure, except the puckering of the V_2O_5 layers (Fig. 4b(5)).

Superpositions of the discharge-charge curves with the stress changes for the fifth and sixth cycles (Fig. 4a, third voltage window) are show in Fig. 5e and f. The same trend is observed until the voltage reaches 2.1 V (Fig. 5e, region I). Upon further discharge, stress in the electrode becomes more compressive (Fig. 5e, region II) due to the more pronounced puckering of the V_2O_5 layer in the γ-phase, as indicated by the augmented asymmetric fringe pattern

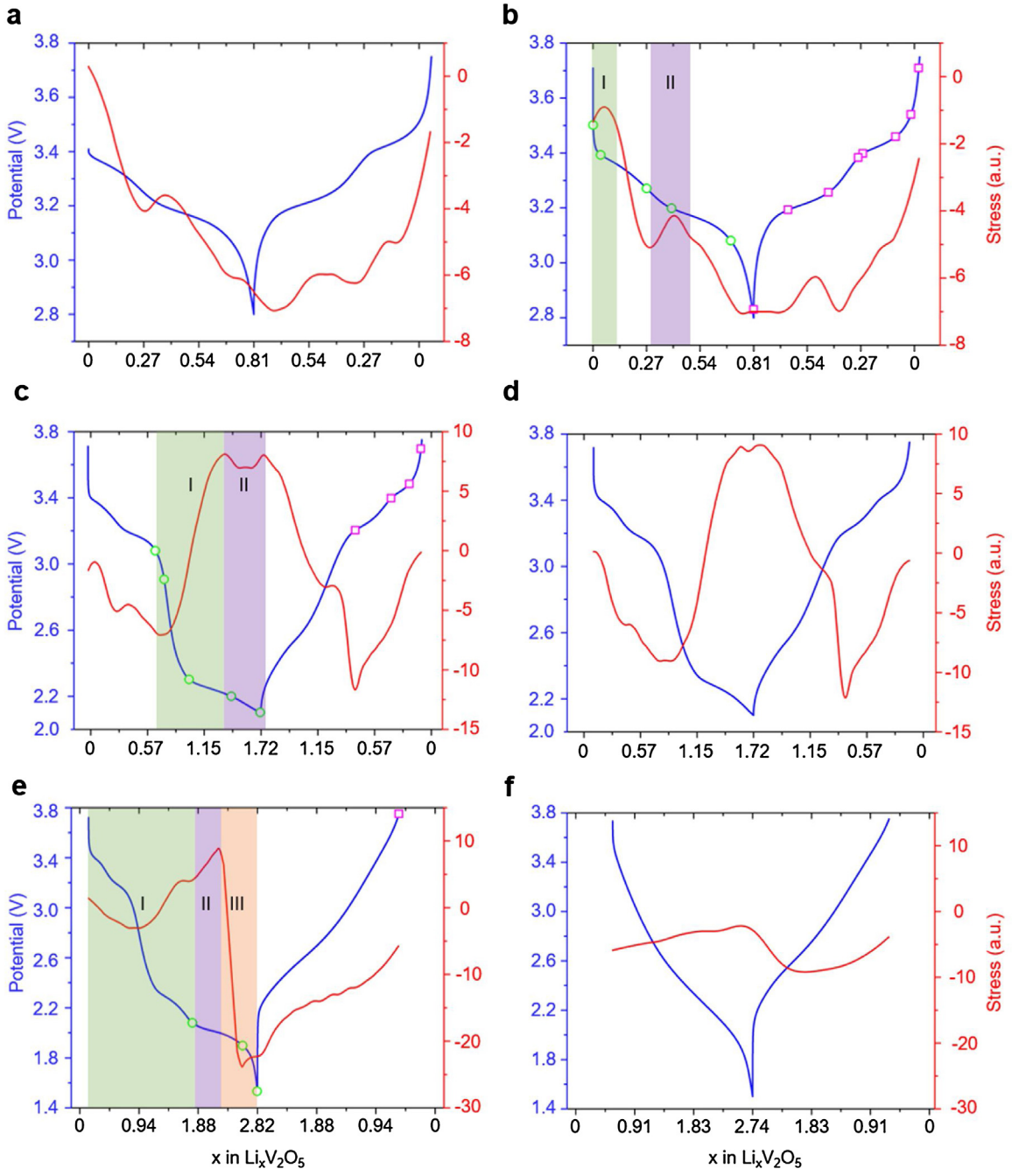

Fig. 5. Qualitative stress characterization. (a,b) Correlation between the stress change and potential variation during discharge-charge of the first and second cycles. (b) Circles in green and rectangles in magenta correspond to the representative points where *in situ* μRaman spectra are analyzed during the second discharge-charge cycle, respectively. (c,d) Correlation between the stress and discharge-charge curves of the third and fourth cycles. (c) Circles in green and rectangles in magenta correspond to representative points where *in situ* μRaman spectra are analyzed during the third discharge-charge cycle, respectively. (e,f) Correlation between the stress change and discharge-charge curves of the fifth and sixth cycles. (e) Circles in green and rectangles in magenta correspond to the representative points where *in situ* μRaman spectra are analyzed during the fifth discharge-charge cycle, respectively.

(Fig. 4b(6)). Still further lithiation induces a sudden change in the stress (Fig. 5e, region III) which rapidly becomes highly tensile, indicating the electrode experiences a dramatic structural transformation from the γ-phase to the tetragonal ω-phase [44]. This tetragonal structure has significantly shorter lattice parameter ($a = 4.1$ Å) compared to the γ-phase (Table 1), which explains the sudden increase in the tensile stress [51]. The ω-phase remains stable even after lithium extraction [47] consistent with the completely different stress change during the sixth cycle (Fig. 5f). Upon lithium insertion, the stress in the electrode becomes more compressive, implying that the $Li_xV_2O_5$ thin film electrode became amorphous [51]. However, upon charge, the stress in the electrode becomes more tensile initially but turns into more compressive stress again in the middle of the process. This may be attributed to the rocksalt-type structure of the ω-phase, resulting in the non-linear stress change. The stress evolution during lithiation is in good agreement with the previously reported

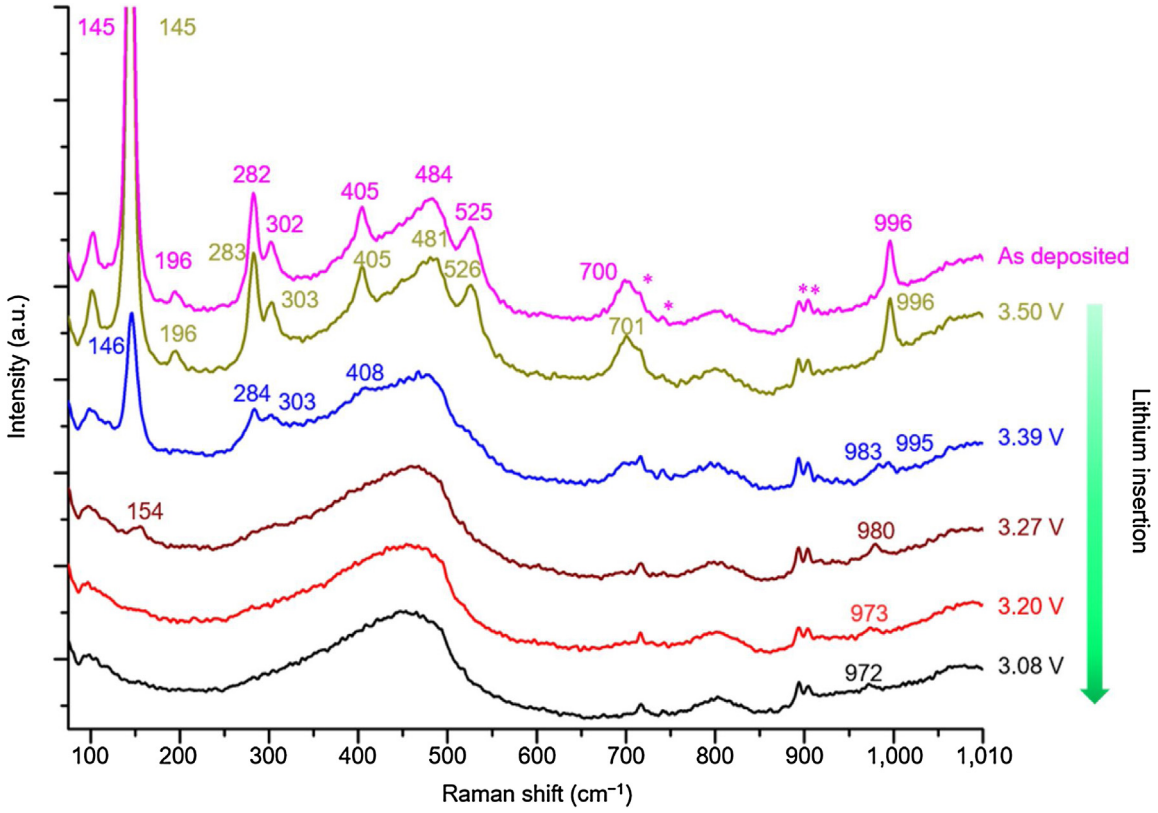

Fig. 6. Detailed view of *in situ* Raman spectra. Detailed view of the *in situ* Raman spectra collected during the second discharge (lithium insertion) process of the $Li_xV_2O_5$ electrode. *Stars denote $LiPF_6$/EC/DMC bands.

phase changes and lattice parameters changes in $Li_xV_2O_5$, confirming the high sensitivity of the platform.

3.3. In situ *analysis of microstructural changes*

Concomitant with the stress measurements, a series of *in situ* Raman spectra of the $Li_xV_2O_5$ electrode are collected and analyzed. The Raman spectra reveal a complete recovery of the pristine V_2O_5 electrode, with regard to relative intensities and peak positions (Supplementary Fig. 6) during the second cycle. This finding is consistent with the high electrochemical reversibility associated with the first voltage window (3.8 – 2.8 V) [52,53].

It is a well-known fact that *in situ* Raman spectroscopy generally suffers from lower signal-to-background ratio upon lithiation in the presence of the electrolyte [3,54,55]. While *ex situ* experiments do not have the added effect of the electrolyte and it is easier to increase the signal-to-background ratio by increasing the Raman accumulation time. This would be ineffective in an *in situ* experiment because the electrolyte background signal would also increase. The *in situ* Raman spectra (Figs. 6 and 8) presented in this work also affected by this phenomenon and as a result, some of the Raman modes are not detected upon lithium insertion. Also, the evolution of the Raman spectra upon lithiation depends on the V_2O_5 material preparation methods. Baddour-Hadjean et al. extensively characterized the V_2O_5 material prepared using different methods (ALD, RF magnetron reactive sputtering, and powders) and the evolution of the Raman spectra differs [3,33,42,56,57]. Depending on the deposition method, preferential growth of the crystallites of V_2O_5 films changes and the structural response varies upon lithiation [56]. In this regards, discussion of the Raman modes identified in this work is compared with the previously reported work where the Raman spectra are measured *in situ* or the V_2O_5 material is prepared using ALD.

During the second cycle discharge process (Fig. 5b), a progressive decrease in the intensity and the Raman shift (145–154 cm^{-1}) are observed for the low frequency vibration modes (mixture of B_{1g} and B_{3g} modes) sensitive to long range order in the $Li_xV_2O_5$ structure (Fig. 6). There is also a considerable loss of intensity for all the Raman peaks in the 195 to 705 cm^{-1} range. The overall loss in Raman intensity during Li insertion into $Li_xV_2O_5$ is consistent with similar loss in intensity during Li extraction from Li_xCoO_2 [58]. In the case of Li_xCoO_2 Li extraction oxidizes Co^{3+} to Co^{4+} forming positive electronic charge carriers [59], while in the case of Li insertion into V_2O_5 V^{5+} reduces to V^{4+} forming negative charge carriers [60]. In either case, the host cathode material

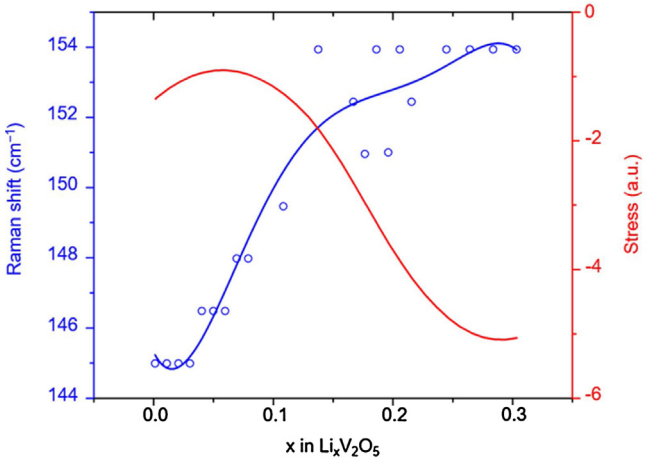

Fig. 7. Raman shift and stress change. Correlation between the peak shift of the Raman translational mode at 145 cm^{-1} (associated with long range order) and the stress change as a function of the lithium insertion in $Li_xV_2O_5$ electrode.

becomes more metallic which substantially reduces the optical skin depth of the Raman excitation light thus reducing intensity. Finally, in the vanadyl stretching mode (996 cm^{-1}), a new peak at 983 cm^{-1} is observed at potential of 3.39 V while the initial peak (996 cm^{-1}) disappears at potential of 3.27 V. The new peak progressively shifts down to 972 cm^{-1} as more Li-ions are inserted into the electrode. These findings are consistent with previous Raman studies of $Li_xV_2O_5$ electrodes [3,33]. The emergence of the new peak at 983 cm^{-1} in the vicinity of the 996 cm^{-1} at potential of 3.39 V has been previously related to a coexistence of the α- and ε-phases [33] and the 973 cm^{-1} peak at the potential of 3.20 V has been ascribed to the presence of ε- and δ-phases [61]. This coexistence of two distinct phases of $Li_xV_2O_5$ as suggested by Raman spectra coincides with the abnormal stress changes observed with our optical stress sensor during the second cycle discharge process (Fig. 5b, region I and II).

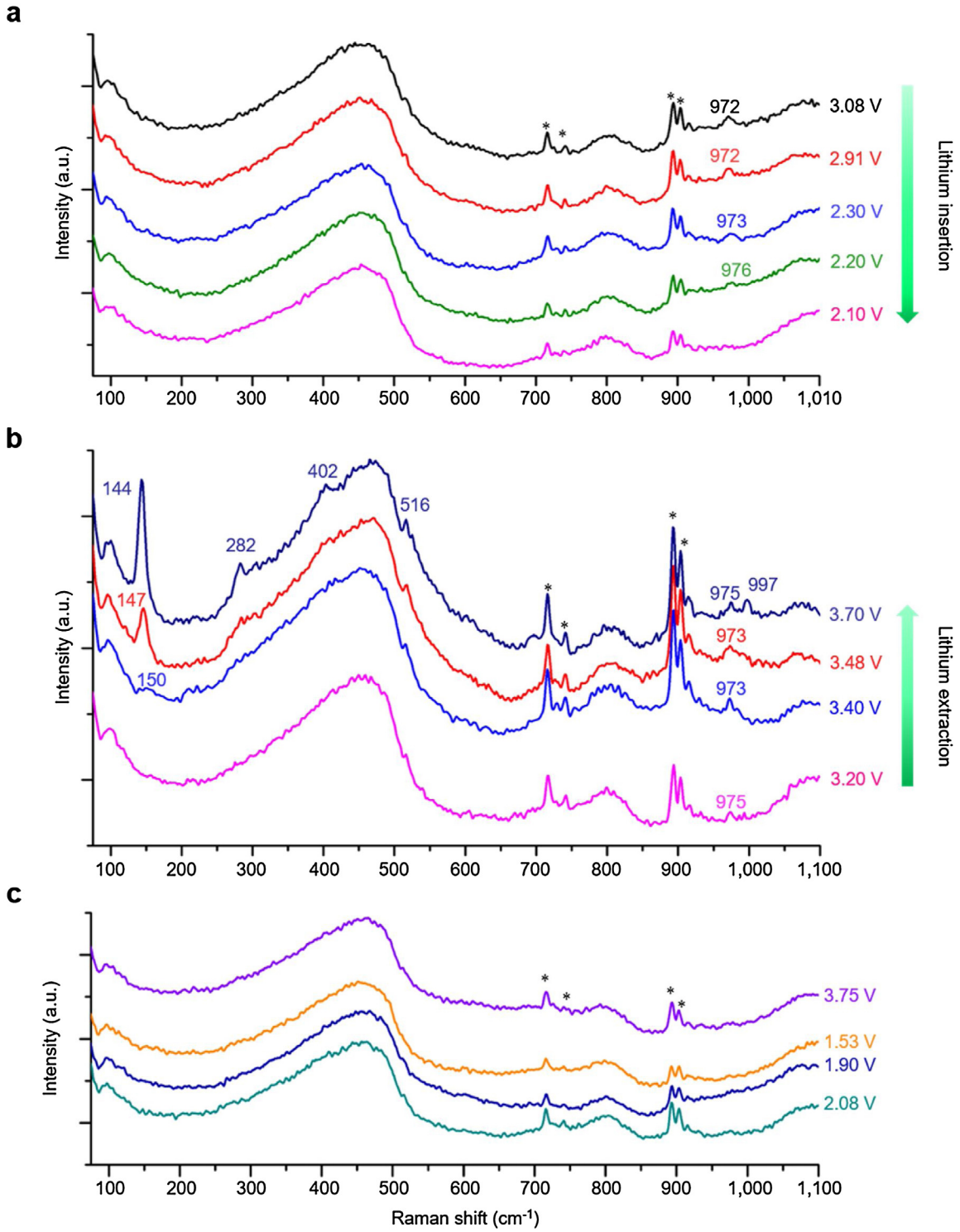

Fig. 8. *In situ* Raman spectra of the third and fifth cycles. Detailed view of the *in situ* Raman spectra collected during the third discharge and charge cycle of the $Li_xV_2O_5$ electrode in the voltage range of (a) 3.08 to 2.10 V and (b) 3.20 to 3.70 V. (c) Detailed view of the *in situ* Raman spectra collected during the fifth discharge and charge cycle of the $Li_xV_2O_5$ electrode. *Stars denote $LiPF_6$/EC/DMC bands.

It has been proposed that the Raman shift from 145 cm^{-1} to 154 cm^{-1} is due to an increase in the restoring force as a consequence of tensile stress in the $Li_xV_2O_5$ film [62]. Our combined approach is now able to confirm this hypothesis by correlating the evolution of the Raman shift at 145 cm^{-1} with the stress change as a function of the lithium insertion in $Li_xV_2O_5$ electrode (Fig. 7). The Raman shifts, which are indicated in blue circles, are quantified by analyzing the Raman spectra measured *in situ* during the second discharge process (Fig. 5b). As the amount of lithium increases during lithiation, the translational mode at 145 cm^{-1} progressively increased to 154 cm^{-1}.

The *in situ* Raman spectra collected for the third discharge and charge processes (Fig. 5c) are shown in Fig. 8a and b. Due to the low signal-to-background ratio in our Raman spectra, not all the Raman modes are identified upon further lithiation. However, the same stretching mode (972 cm^{-1}, Fig. 6 at 3.08 V) is observed at 3.08 V (Fig. 8a). Also, the peak shifts to higher wavenumbers upon further lithiation, which is also observed in the *ex situ* Raman study of ALD-deposited V_2O_5 during δ- to γ-phase transformation [61], and completely disappears at 2.10 V (Fig. 8a). These spectral changes can be attributed to irreversible loss in crystallinity during formation of the γ-phase [45]. This irreversible change is also evidenced by the fact that some of the modes (196, 302, 484, and 700 cm^{-1}) are no longer observed after the electrode is charged back to 3.70 V (lithium extraction) (Fig. 8b). Similarly, the peaks at 144 cm^{-1} and vanadyl stretching mode at 997 cm^{-1} do not recover their original intensity, indicating high degree of disorder in the V_2O_5 layer. Finally, the peak at 975 cm^{-1} associated with the γ-phase is still observed even after all the lithium extraction (Fig. 8b, 3.70 V), which is consistent with the irreversibility of this phase [43].

The *in situ* Raman spectra collected for the fifth discharge and charge processes (Fig. 5e) shown in Fig. 8c display no discernable peaks, indicating that Raman is not able to detect the γ- to ω-phase transition in contrast to the already shown results with the *in situ* optical stress sensor (Fig. 4(6), (7), (8)) (Fig. 5e, region III). Even after the electrode is charged back to 3.75 V, no detectable peaks are found, suggesting that the electrochemically formed weakly crystalline ω-phase has a nearly amorphous structure and remains in this metastable state even all the lithium extraction [47].

The *in situ* μRaman spectroscopy measurement results achieved using our platform match well with the previously Raman study of V_2O_5 electrodes [3,33,61], indicating this technique is capable of characterizing both the stress and microstructural changes concurrently. Fully reversible α- to δ-phase transitions are observed as well as the irreversible transformation in the γ-phase are evidenced in a single, continuous experiment for the first time using *in situ* μRaman spectroscopy technique.

4. Conclusion

A full understanding of the stress-microstructure relation in the Li/V_2O_5 system is challenging due to the complex physico-chemical transformations during Li insertion/extraction reactions [3]. We have shown that the combination of our MEMS optical stress sensor with commercially available Raman microspectroscopy setup allows *in situ* analysis on the qualitative stress changes and characterization of the microstructural evolutions in different phases of the $Li_xV_2O_5$ electrode. The integrated setup demonstrates a unique advantage in the visualization of the phase evolutions in the $Li_xV_2O_5$ electrode which enables confirmation of the pronounced puckering in the V_2O_5 electrode structure due to phase evolution and formation of the rocksalt-type structure upon further discharge. We have also shown that the electrode experiences a dramatic change when the phase of the electrode is transformed from γ- to ω-phase. The stress variation with different phases of the electrode are also characterized through analysis of the interference patterns and corresponding structure evolutions using μRaman spectroscopy which indicates fully reversible structural changes from the α- to δ-phase, irreversible γ-phase with the permanent bond breaking, and weakly crystallized ω-phase.

All these results are achieved through an one-time experiment in an unified setup. By selecting the complex Li/V_2O_5 as a model system to demonstrate the utility of the MEMS optical stress sensor and methodology, our approach demonstrates its applicability to other battery electrode materials. Thus, our approach opens up a new way to investigate critical factors affecting LIB performance, which is also applicable to various thin film LIB electrodes.

Acknowledgements

This work was supported as part of the Nanostructures for Electrical Energy Storage (NEES), an Energy Frontier Research Center funded by the U.S. Department of Energy, Office of Science, Basic Energy Sciences under Award number DESC0001160. The authors acknowledge the staff at Maryland Nanocenter, AIMLab, and Surface Analysis Center. Sandia National Laboratories is a multi-program laboratory managed and operated by Sandia Corporation, a wholly owned subsidiary of Lockheed Martin Corporation, for the U.S. Department of Energy's National Nuclear Security Administration under contract DE-AC04-94AL85000.

Appendix A. Supplementary data

Supplementary data associated with this article can be found, in the online version, at http://dx.doi.org/10.1016/j.electacta.2017.04.160.

References

[1] F.T. Wagner, B. Lakshmanan, M.F. Mathias, Electrochemistry and the Future of the Automobile, J. Phys. Chem. Lett. 1 (2010) 2204–2219, doi:http://dx.doi.org/10.1021/jz100553m.
[2] J. Cabana, L. Monconduit, D. Larcher, M.R. Palacín, Beyond Intercalation-Based Li-Ion Batteries: The State of the Art and Challenges of Electrode Materials Reacting Through Conversion Reactions, Adv. Mater. 22 (2010) E170–E192, doi:http://dx.doi.org/10.1002/adma.201000717.
[3] R. Baddour-Hadjean, J.-P. Pereira-Ramos, Raman Microspectrometry Applied to the Study of Electrode Materials for Lithium Batteries, Chem. Rev. 110 (2010) 1278–1319, doi:http://dx.doi.org/10.1021/cr800344k.
[4] M.V. Reddy, G.V. Subba Rao, B.V.R. Chowdari, Metal Oxides and Oxysalts as Anode Materials for Li Ion Batteries, Chem. Rev. 113 (2013) 5364–5457, doi:http://dx.doi.org/10.1021/cr3001884.
[5] J.-M. Tarascon, M. Armand, Issues and challenges facing rechargeable lithium batteries, Nature 414 (2001) 359–367, doi:http://dx.doi.org/10.1038/35104644.
[6] M.T. McDowell, S.W. Lee, W.D. Nix, Y. Cui, 25th anniversary article: Understanding the lithiation of silicon and other alloying anodes for lithium-ion batteries, Adv. Mater. 25 (2013) 4966–4985, doi:http://dx.doi.org/10.1002/adma.201301795.
[7] R. Hausbrand, G. Cherkashinin, H. Ehrenberg, M. Gröting, K. Albe, C. Hess, et al., Fundamental degradation mechanisms of layered oxide Li-ion battery cathode materials: Methodology, insights and novel approaches, Mater. Sci. Eng. B. 192 (2015) 3–25, doi:http://dx.doi.org/10.1016/j.mseb.2014.11.014.
[8] M.J. Chon, V.A. Sethuraman, A. McCormick, V. Srinivasan, P.R. Guduru, Real-time measurement of stress and damage evolution during initial lithiation of crystalline silicon, Phys Rev Lett. 107 (2011) 45503. http://dx.doi.org/.
[9] V.A. Sethuraman, M.J. Chon, M. Shimshak, V. Srinivasan, P.R. Guduru, In situ measurements of stress evolution in silicon thin films during electrochemical lithiation and delithiation, J. Power Sources. 195 (2010) 5062–5066, doi:http://dx.doi.org/10.1016/j.jpowsour.2010.02.013.
[10] K.Y. Chung, K.-B. Kim, Investigation of Structural Fatigue in Spinel Electrodes Using In Situ Laser Probe Beam Deflection Technique, J. Electrochem. Soc. 149 (2002) A79–A85, doi:http://dx.doi.org/10.1149/1.1426396.
[11] H. Mukaibo, T. Momma, Y. Shacham-Diamand, T. Osaka, M. Kodaira, In Situ Stress Transition Observations of Electrodeposited Sn-Based Anode Materials for Lithium-Ion Secondary Batteries, Electrochem. Solid-State Lett. 10 (2007) A70, doi:http://dx.doi.org/10.1149/1.2426410.
[12] S.-I. Pyun, K.-H. Kim, J.-N. Han, Analysis of stresses generated during hydrogen extraction from and injection into Ni(OH)2/NiOOH film electrode, J. Power

Sources. 91 (2000) 92–98, doi:http://dx.doi.org/10.1016/S0378-7753(00)00464-X.
[13] S.J. Lee, J.K. Lee, S.H. Chung, H.Y. Lee, S.M. Lee, H.K. Baik, Stress effect on cycle properties of the silicon thin-film anode, J. Power Sources. 97 (2001) 191–193.
[14] V.A. Sethuraman, M.J. Chon, M. Shimshak, N. Van Winkle, P.R. Guduru, In situ measurement of biaxial modulus of Si anode for Li-ion batteries, Electrochem. Commun. 12 (2010) 1614–1617, doi:http://dx.doi.org/10.1016/j.elecom.2010.09.008.
[15] E.M.C. Jones, M.N. Silberstein, S.R. White, N.R. Sottos, In Situ Measurements of Strains in Composite Battery Electrodes during Electrochemical Cycling, Exp. Mech. 54 (2014) 971–985, doi:http://dx.doi.org/10.1007/s11340-014-9873-3.
[16] V.A. Sethuraman, N. Van Winkle, D.P. Abraham, A.F. Bower, P.R. Guduru, Real-time stress measurements in lithium-ion battery negative-electrodes, J. Power Sources. 206 (2012) 334–342, doi:http://dx.doi.org/10.1016/j.jpowsour.2012.01.036.
[17] X.H. Liu, J.Y. Huang, In situ TEM electrochemistry of anode materials in lithium ion batteries, Energy Environ. Sci. 4 (2011) 3844–3860, doi:http://dx.doi.org/10.1039/C1EE01918J.
[18] J.Y. Huang, L. Zhong, C.M. Wang, J.P. Sullivan, W. Xu, L.Q. Zhang, et al., In Situ Observation of the Electrochemical Lithiation of a Single SnO2 Nanowire Electrode, Science 330 (2010) 1515–1520, doi:http://dx.doi.org/10.1126/science.1195628 (80-.).
[19] F. Wang, H.-C. Yu, M.-H. Chen, L. Wu, N. Pereira, K. Thornton, et al., Tracking lithium transport and electrochemical reactions in nanoparticles, Nat Commun. 3 (2012) 1201, doi:http://dx.doi.org/10.1038/ncomms2185.
[20] M. Balasubramanian, X. Sun, X.Q. Yang, J. McBreen, In situ X-ray diffraction and X-ray absorption studies of high-rate lithium-ion batteries, J. Power Sources. 92 (2001) 1–8, doi:http://dx.doi.org/10.1016/S0378-7753(00)00493-6.
[21] T.D. Hatchard, J.R. Dahn, In Situ XRD and Electrochemical Study of the Reaction of Lithium with Amorphous Silicon, J. Electrochem. Soc. 151 (2004) A838–A842, doi:http://dx.doi.org/10.1149/1.1739217.
[22] J. Li, J.R. Dahn, An In Situ X-Ray Diffraction Study of the Reaction of Li with Crystalline Si, J. Electrochem. Soc. 154 (2007) A156–A161, doi:http://dx.doi.org/10.1149/1.2409862.
[23] K.J. Rhodes, R. Meisner, M. Kirkham, N. Dudney, C. Daniel, In Situ XRD of Thin Film Tin Electrodes for Lithium Ion Batteries, J. Electrochem. Soc. 159 (2012) A294–A299, doi:http://dx.doi.org/10.1149/2.077203jes.
[24] W.-S. Yoon, M. Balasubramanian, K.Y. Chung, X.-Q. Yang, J. McBreen, C.P. Grey, et al., Investigation of the Charge Compensation Mechanism on the Electrochemically Li-Ion Deintercalated Li1-xCo1/3Ni1/3Mn1/3O2 Electrode System by Combination of Soft and Hard X-ray Absorption Spectroscopy, J. Am. Chem. Soc. 127 (2005) 17479–17487, doi:http://dx.doi.org/10.1021/ja0530568.
[25] X. Liu, D. Wang, G. Liu, V. Srinivasan, Z. Liu, Z. Hussain, et al., Distinct charge dynamics in battery electrodes revealed by in situ and operando soft X-ray spectroscopy, Nat Commun. 4 (2013), doi:http://dx.doi.org/10.1038/ncomms3568.
[26] B. Key, R. Bhattacharyya, M. Morcrette, V. Seznéc, J.-M. Tarascon, C.P. Grey, Real-Time NMR Investigations of Structural Changes in Silicon Electrodes for Lithium-Ion Batteries, J. Am. Chem. Soc. 131 (2009) 9239–9249, doi:http://dx.doi.org/10.1021/ja8086278.
[27] K. Ogata, E. Salager, C.J. Kerr, A.E. Fraser, C. Ducati, A.J. Morris, et al., Revealing lithium-silicide phase transformations in nano-structured silicon-based lithium ion batteries via in situ NMR spectroscopy, Nat Commun 5 (2014), doi:http://dx.doi.org/10.1038/ncomms4217.
[28] X.-L. Wang, K. An, L. Cai, Z. Feng, S.E. Nagler, C. Daniel, et al., Visualizing the chemistry and structure dynamics in lithium-ion batteries by in-situ neutron diffraction, Sci. Rep. 2 (2012). http://www.nature.com/srep/2012/121019/srep00747/abs/srep00747.html#supplementary-information.
[29] C.M. Burba, R. Frech, Modified Coin Cells for xV2O5 for Lithium Rechargeable Batteries, Appl. Spectrosc. 60 (2006) 490–493, doi:http://dx.doi.org/10.1366/000370206777412167.
[30] J. Wu, G.K.P. Dathar, C. Sun, M.G. Theivanayagam, D. Applestone, A.G. Dylla, et al., In situ Raman spectroscopy of LiFePO4: size and morphology dependence during charge and self-discharge, Nanotechnology. 24 (2013) 424009, doi:http://dx.doi.org/10.1088/0957-4484/24/42/424009.
[31] D.V. Esposito, J.B. Baxter, J. John, N.S. Lewis, T.P. Moffat, T. Ogitsu, et al., Methods of photoelectrode characterization with high spatial and temporal resolution, Energy Environ Sci. 8 (2015) 2863–2885, doi:http://dx.doi.org/10.1039/C5EE00835B.
[32] L.J. Hardwick, P.W. Ruch, M. Hahn, W. Scheifele, R. Kötz, P. Novák, In situ Raman spectroscopy of insertion electrodes for lithium-ion batteries and supercapacitors: First cycle effects, J. Phys. Chem. Solids. 69 (2008) 1232–1237, doi:http://dx.doi.org/10.1016/j.jpcs.2007.10.017.
[33] R. Baddour-Hadjean, C. Navone, J.P. Pereira-Ramos, In situ Raman microspectrometry investigation of electrochemical lithium intercalation into sputtered crystalline V2O5 thin films, Electrochim. Acta. 54 (2009) 6674–6679, doi:http://dx.doi.org/10.1016/j.electacta.2009.06.052.
[34] T. Gross, C. Hess, Spatially-Resolved In Situ Raman Analysis of LiCoO2 Electrodes, ECS Trans. 61 (2014) 1–9, doi:http://dx.doi.org/10.1149/06112.0001ecst.
[35] L.J. Hardwick, M. Holzapfel, P. Novák, L. Dupont, E. Baudrin, Electrochemical lithium insertion into anatase-type TiO2: An in situ Raman microscopy investigation, Electrochim. Acta. 52 (2007) 5357–5367, doi:http://dx.doi.org/10.1016/j.electacta.2007.02.050.
[36] H. Kanoh, W. Tang, K. Ooi, In Situ Raman Spectroscopic Study on Electroinsertion of Li + into a Pt/λ - MnO2 Electrode in Aqueous Solution, Electrochem. Solid-State Lett. 1 (1998) 17–19, doi:http://dx.doi.org/10.1149/1.1390620.
[37] J. Lei, F. McLarnon, R. Kostecki, In Situ Raman Microscopy of Individual LiNi0.8Co0.15Al0.05O2 Particles in a Li-Ion Battery Composite Cathode, J. Phys. Chem. B. 109 (2005) 952–957, doi:http://dx.doi.org/10.1021/jp046027c.
[38] A. Sakunthala, M.V. Reddy, S. Selvasekarapandian, B.V.R. Chowdari, P.C. Selvin, Energy storage studies of bare and doped vanadium pentoxide, (V1.95M0.05)O5, M = Nb, Ta, for lithium ion batteries, Energy Environ Sci. 4 (2011) 1712–1725, doi:http://dx.doi.org/10.1039/C0EE00513D.
[39] E. Pomerantseva, H. Jung, M. Gnerlich, S. Baron, K. Gerasopoulos, R. Ghodssi, A MEMS platform for in situ, real-time monitoring of electrochemically induced mechanical changes in lithium-ion battery electrodes, J. Micromechanics Microengineering. 23 (2013) 114018, doi:http://dx.doi.org/10.1088/0960-1317/23/11/114018.
[40] X. Chen, E. Pomerantseva, P. Banerjee, K. Gregorczyk, R. Ghodssi, G. Rubloff, Ozone-Based Atomic Layer Deposition of Crystalline V2O5 Films for High Performance Electrochemical Energy Storage, Chem. Mater. 24 (2012) 1255–1261, doi:http://dx.doi.org/10.1021/cm202901z.
[41] S.T. Koev, W.E. Bentley, R. Ghodssi, Interferometric readout of multiple cantilever sensors in liquid samples, Sensors Actuators B Chem. 146 (2010) 245–252, doi:http://dx.doi.org/10.1016/j.snb.2010.02.038.
[42] R. Baddour-Hadjean, J.P. Pereira-Ramos, C. Navone, M. Smirnov, Raman Microspectrometry Study of Electrochemical Lithium Intercalation into Sputtered Crystalline V2O5 Thin Films, Chem. Mater. 20 (2008) 1916–1923, doi:http://dx.doi.org/10.1021/cm702979k.
[43] J.M. Cocciantelli, J.P. Doumerc, M. Pouchard, M. Broussely, J. Labat, Crystal chemistry of electrochemically inserted LixV2O5, J. Power Sources. 34 (1991) 103–111, doi:http://dx.doi.org/10.1016/0378-7753(91)85029-V.
[44] C. Delmas, H. Cognac-Auradou, J.M. Cocciantelli, M. Ménétrier, J.P. Doumerc, The LixV2O5 system: An overview of the structure modifications induced by the lithium intercalation, Solid State Ionics. 69 (1994) 257–264, doi:http://dx.doi.org/10.1016/0167-2738(94)90414-6.
[45] J.M. Cocciantelli, P. Gravereau, J.P. Doumerc, M. Pouchard, P. Hagenmuller, On the preparation and characterization of a new polymorph of V2O5, J. Solid State Chem. 93 (1991) 497–502, doi:http://dx.doi.org/10.1016/0022-4596(91)90323-A.
[46] C. Leger, S. Bach, P. Soudan, J.P. Pereira-Ramos, Structural and Electrochemical Properties of (Lix V2O5 (0.4 ≤ x ≤ 3) as Rechargeable Cathodic Material for Lithium Batteries, J. Electrochem. Soc. 152 (2005) A236–A241, doi:http://dx.doi.org/10.1149/1.1836155.
[47] C. Delmas, S. Brèthes, M. Ménétrier, ω-LixV2O5 — a new electrode material for rechargeable lithium batteries, J. Power Sources. 34 (1991) 113–118, doi:http://dx.doi.org/10.1016/0378-7753(91)85030-Z.
[48] E. Hatzikraniotis, C.L. Mitsas, D.I. Siapkas, Differential Capacity Analysis, a Tool to Examine the Performance of Graphites for Li-Ion Cells, in: C. Julien, Z. Stoynov (Eds.), Mater. Lithium-Ion Batter, Springer, Netherlands, Dordrecht, 2000, pp. 529–534, doi:http://dx.doi.org/10.1007/978-94-011-4333-2_35.
[49] A.J. Smith, J.R. Dahn, Delta Differential Capacity Analysis, J. Electrochem. Soc. 159 (2012) A290–A293, doi:http://dx.doi.org/10.1149/2.076203jes.
[50] E.A. Meulenkamp, W. van Klinken, A.R. Schlatmann, In-situ X-ray diffraction of Li intercalation in sol–gel V2O5 films, Solid State Ionics. 126 (1999) 235–244, doi:http://dx.doi.org/10.1016/S0167-2738(99)00243-X.
[51] J. Scarminio, A. Talledo, A.A. Andersson, S. Passerini, F. Decker, Stress and electrochromism induced by Li insertion in crystalline and amorphous V2O5 thin film electrodes, Electrochim. Acta. 38 (1993) 1637–1642, doi:http://dx.doi.org/10.1016/0013-4686(93)85053-2.
[52] C. Navone, J.P. Pereira-Ramos, R. Baddour-Hadjean, R. Salot, High-Capacity Crystalline V2O5 Thick Films Prepared by RF Sputtering as Positive Electrodes for Rechargeable Lithium Microbatteries, J. Electrochem. Soc. 153 (2006) A2287–A2293, doi:http://dx.doi.org/10.1149/1.2358852.
[53] C. Navone, R. Baddour-Hadjean, J.P. Pereira-Ramos, R. Salot, A kinetic study of electrochemical lithium insertion into oriented V2O5 thin films prepared by rf sputtering, Electrochim. Acta. 53 (2008) 3329–3336, doi:http://dx.doi.org/10.1016/j.electacta.2007.11.061.
[54] R. Baddour-Hadjean, J.-P. Pereira-Ramos, Raman Investigation of Cathode Materials for Lithium Batteries, Wiley-VCH Verlag GmbH & Co. KGaA, 2010, doi:http://dx.doi.org/10.1002/9783527629022.ch6.
[55] P. Novák, J.-C. Panitz, F. Joho, M. Lanz, R. Imhof, M. Coluccia, Advanced in situ methods for the characterization of practical electrodes in lithium-ion batteries, J. Power Sources. 90 (2000) 52–58, doi:http://dx.doi.org/10.1016/S0378-7753(00)00447-X.
[56] R. Baddour-Hadjean, E. Raekelboom, J.P. Pereira-Ramos, New Structural Characterization of the LixV2O5 System Provided by Raman Spectroscopy, Chem. Mater. 18 (2006) 3548–3556, doi:http://dx.doi.org/10.1021/cm060540g.
[57] R. Baddour-Hadjean, A. Marzouk, J.P. Pereira-Ramos, Structural modifications of LixV2O5 in a composite cathode (0 ≤ x<2) investigated by Raman microspectrometry, J. Raman Spectrosc. 43 (2012) 153–160, doi:http://dx.doi.org/10.1002/jrs.2984.
[58] Y. Park, N.H. Kim, J.Y. Kim, I.-Y. Eom, Y.U. Jeong, M.S. Kim, et al., Surface characterization of the high voltage LiCoO2/Li cell by X-ray photoelectron spectroscopy and 2D correlation analysis, Vib. Spectrosc. 53 (2010) 60–63, doi:http://dx.doi.org/10.1016/j.vibspec.2010.01.004.
[59] A. Milewska, K. Świerczek, J. Tobola, F. Boudoire, Y. Hu, D.K. Bora, et al., The nature of the nonmetal–metal transition in LixCoO2 oxide, Solid State Ionics. 263 (2014) 110–118, doi:http://dx.doi.org/10.1016/j.ssi.2014.05.011.

[60] M.S. Al-Assiri, M.M. El-Desoky, A. Alyamani, A. Al-Hajry, A. Al-Mogeeth, A.A. Bahgat, Structural and transport properties of Li-intercalated vanadium pentoxide nanocrystalline films, Philos. Mag. 90 (2010) 3421–3439, doi:http://dx.doi.org/10.1080/14786435.2010.485938.
[61] R. Baddour-Hadjean, V. Golabkan, J.P. Pereira-Ramos, A. Mantoux, D. Lincot, A Raman study of the lithium insertion process in vanadium pentoxide thin films deposited by atomic layer deposition, J. Raman Spectrosc. 33 (2002) 631–638, doi:http://dx.doi.org/10.1002/jrs.893.
[62] C. Julien, I. Ivanov, A. Gorenstein, Vibrational modifications on lithium intercalation in V2O5 films, Mater. Sci. Eng. B. 33 (1995) 168–172, doi:http://dx.doi.org/10.1016/0921-5107(95)80032-8.